

FIG. 6.9. Maps showing (a) duration anomaly for the 2016/17 sea ice season in days and (b) duration trend for 1979/80–2016/17 in days yr⁻¹. The black contour in (b) delineates those trends with significance at the $p < 0.01$ significance level.

the regional rate of ice retreat, particularly in the Bellingshausen–Amundsen (60°–120°W) and Weddell (30°W–30°E) Seas where slower and faster retreat occurred, respectively (Fig. 6.8a).

These austral springtime sea ice distribution changes are consistent with the influence of the relatively weak La Niña developing within the tropical Pacific in early November 2017 (see Section 4b), which changed the position of the higher-latitude southern jet streams and hence the cyclonicity around the Antarctic continental edge (Yuan 2004; Stammerjohn et al. 2008). Thus, SIE towards the end of the year and within the Weddell Sea was, in some areas, more than six standard deviations below average. Elsewhere, SIE was close to average, although small pockets of greater-than-average SIE existed within the Amundsen Sea and western Pacific sector (~110°–150°E) associated with wind-driven compaction of the sea ice cover and lower-than-normal SSTs near these regions.

The long-term trend for Antarctic sea ice is regionally and seasonally variable: increased SIE and longer seasonal duration within the Ross and Weddell Seas, and decreased SIE and shorter duration in the Bellingshausen–Amundsen Seas (e.g., Fig. 6.9b for sea ice duration trends over 1979/80–2016/17; see Comiso et al. 2017 for sea ice extent trends). For SIE these changes are largest during January–May (Hobbs et al. 2016). Apart from some areas of the Amundsen Sea, the regional pattern of sea ice coverage during 2017, described above, was in contrast to this long-term trend (Fig. 6.9a), particularly in much of the Ross

Sea and the Weddell Sea through the end of March.

f. Southern Ocean—S. Swart, K. Johnson, M. R. Mazloff, A. Meijers, M. P. Meredith, L. Newman, and J.-B. Sallée

In the climate system, the Southern Ocean is disproportionately important when it comes to its storage of heat and carbon. Modification of the upper Southern Ocean could have significant implications for the rate and magnitude of air–sea fluxes (of heat and carbon) and for the ventilation of the ocean interior, thereby altering the effects of climate warming on the ocean system as a whole. Here, we evaluate the state of the Southern Ocean in 2017 by first assessing the upper ocean as the interface between the atmosphere and ocean interior.

We then discuss the changes in intermediate to deep water masses, which are critical pathways to moving heat and carbon to the ocean interior where it will (in general) remain for decades to centuries. Lastly, we report on the status of ocean acidification in the Southern Ocean using newly available biogeochemical observations.

1) UPPER OCEAN

By utilizing all available 2017 hydrographic profiles (40 816 from Argo floats and 11 916 from tagged seals), anomalies of mixed layer depth (MLD) and mixed layer (ML) temperature and salinity (Figs. 6.10a–c) were computed from the climatological (2000–2010) seasonal cycle (see Pellichero et al. 2017). During 2017, the most significant observation is the shallower MLDs (negative anomalies) occurring in the Pacific sector, particularly within the Antarctic Circumpolar Current (ACC), where MLDs are more than 100 m shallower than the climatology. Meanwhile, the Atlantic and Indian sectors are characterized by mixed MLD anomalies.

In contrast to anomalies reported for 2015 and 2016 (Sallée et al. 2016; Mazloff et al. 2017), a markedly warmer ML (Fig. 6.10b) was observed throughout most of the Southern Ocean in 2017, except for the northern subantarctic region of the Atlantic sector. In further contrast, positive Southern Ocean ML temperature anomalies in 2015 were juxtaposed against negative anomalies to the north, indicating a north–south dipole separated by the ACC (Sallée et al. 2016), while in

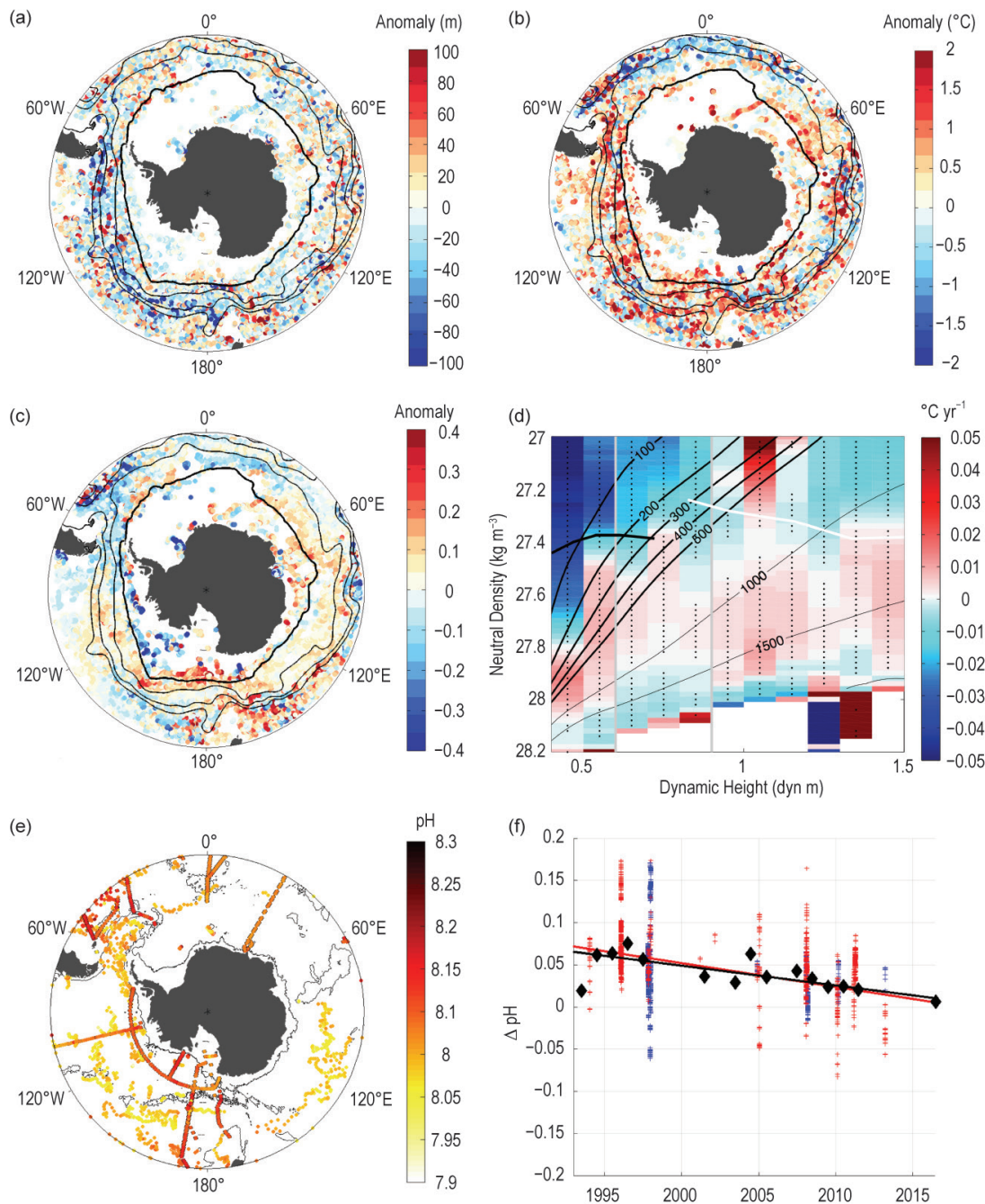


FIG. 6.10. (a) Mixed layer depth anomaly (m) in 2017 from the climatological seasonal cycle. The thin black contours represent the main ACC fronts from north to south: northern Subantarctic Front (SAF), main SAF, Polar Front (PF). The thick black contour is the Sep. climatological sea ice extent. (b) Same as (a) but for mixed layer temperature (°C). (c) Same as (a) but for mixed layer absolute salinity. (d) Circumpolar average trend in potential temperature (in °C yr⁻¹) from Argo float data (seasonal cycle removed), oriented along constant dynamic height and isopycnal surfaces. The thick solid black contour is the T-min layer and the white contour is the S-min layer. Constant pressure surfaces are indicated. Vertical lines indicate the position of the PF (left) and SAF (right). Dots indicate trends in potential temperature significant at the 95% level. (e) Observed upper 30-m pH (black outlined colored dots) from the GLODAPv2 database (Key et al. 2015) spanning 1992–2013 and the SOCCOM pH observations in 2017 (colored dots without outlines). The 3000-m bathymetry contour is shown in black. (f) Changes in pH via two different methods: black diamonds are annual averaged GLODAPv2 comparisons (1992–2013) to all SOCCOM float data (2014–17), while red/blue pluses denote the discrete GLODAPv2 comparisons to only 2017 float data and all other float data, respectively (based on criteria explained in the text). The black and red lines are the linear fit to the respective color markers.

2016, ML temperature anomalies defined a quadrupole delimited by ocean basins (Mazloff et al. 2017).

In 2017 warmer ML temperatures north of the mean September ice edge (thick black contour in Figs. 6.10a-c) generally coincided with shallower MLDs (negative anomalies; Fig. 6.10a) and increased ocean stratification (not shown). However, deeper MLDs (positive anomalies) appearing in the Indian sector of the Southern Ocean (centered on 60°E near the mean September ice edge) coincided with anomalously saline mixed layers (Fig. 6.10c) and reduced ocean stratification (not shown). South of the ACC (and mean September ice edge) there are fewer observations, but overall the data suggest a negative MLD anomaly (shallower) in the West Antarctic sector together with strongly negative ML salinity (fresher) and positive (higher) ML temperature anomalies. These fresher MLs may be linked with a long-term increase in wind-driven transport of freshwater northward (Haumann et al. 2016) and/or increased sea ice melt in summer (February) 2017 (Section 6e). From the Maud Rise region (~3°E) towards East Antarctica positive ML salinity anomalies (Fig. 6.10c) were observed, which resulted in weak stratification. These changes may be linked to the anomalously low sea ice conditions experienced in the eastern Weddell Sea (Section 6e) together with the recent re-emergence of the Maud Rise polynya and its associated impacts on the upper ocean via enhanced air-sea exchanges and ventilation of warmer, saltier interior water masses (see Sidebar 6.1).

2) INTERMEDIATE OCEAN

Significant thermohaline changes are occurring below the surface layers of the Southern Ocean. Due to the slow time scales of these changes (unlike the more temporally sensitive surface mixed layer properties just described), it is more appropriate to discuss multi-year changes (2002–16). The gravest empirical mode (GEM; see methods in Meijers et al. 2011; Swart et al. 2010), a highly effective method to reconstruct subsurface property fields from sea surface height, is used to map thermal changes at intermediate depths (thermocline depth to 2000 m). The GEM uses a current inventory of all Argo float profiles (2002 to 2016) to derive circumpolar-averaged potential temperature trends approximately oriented along stream-following dynamic height contours, here shown on constant isopycnal surfaces (Fig. 6.10d). Such a coordinate choice removes aliasing and trends due to frontal movements and vertical heave.

Overall, there was a consistent warming of up to $0.02^{\circ}\text{C yr}^{-1}$ (Fig. 6.10d) and salinification (not shown:

$27.6\text{--}28\text{ kg m}^{-3}$) of the densest Antarctic Intermediate Water (AAIW) and Circumpolar Deep Water (CDW) throughout the Southern Ocean over 2002–16. This may be related to changes in westerly winds (due to long-term increases in the SAM; Böning et al. 2008). Lying above these depths, two fairly distinct negative trends were observed, one north of the Polar Front ($> 0.8\text{ dyn m}$), which indicates cooling of the upper AAIW and Subantarctic Mode Water (SAMW; $-0.01^{\circ}\text{C yr}^{-1}$), and the other south of the Polar Front, which indicates relatively strong cooling and freshening of winter and surface water (e.g., Haumann et al. 2016) ranging from -0.015° to $-0.05^{\circ}\text{C yr}^{-1}$. The cooling of SAMW in the northern ACC does not contradict the general warming trend observed beyond the northern ACC, as this may be related to increased volume and hence heat content of SAMW and AAIW predominantly caused by wind-driven changes, namely increased wind stress curl (Gao et al. 2018).

3) BIOGEOCHEMICAL STATUS: CONTINUED OCEAN ACIDIFICATION

The new Southern Ocean Carbon and Climate Observations and Modeling project (SOCCOM) array currently has 105 active profiling floats, allowing a characterization of ocean pH variability at shorter time scales and higher spatial resolution. Ocean pH is decreasing as anthropogenic CO_2 enters the ocean and forms carbonic acid (causing ocean acidification). Ocean acidification challenges the viability of organisms producing CaCO_3 shells and has fundamental impacts on the ocean carbon cycle.

Observed pH in the upper 30 m from the GLODAPv2 database (1992–2013 observations as black outlined colored dots in Fig. 6.10e; Key et al. 2015; Olsen et al. 2016) is compared to SOCCOM pH observations in 2017 (colored dots without black outlines). It is qualitatively apparent that the GLODAPv2 estimates have higher pH. Two methods were used to quantify these differences. For the first method, all upper 150-m GLODAPv2 observations from 1992 to 2013 were used, and float observations (from 2014 to 2017) that were within 20-km and 5-m depth of the GLODAPv2 observations were identified. Differences in pH between GLODAPv2 and float observations were determined and bin-averaged for each year of GLODAPv2 observations (black diamonds in Fig. 6.10f); any year with less than five matches was eliminated. (The additional data point for 2016 shows the mean offset between float pH and hydrocast pH, the latter acquired during float deployments; Johnson et al. 2017). A second method identified all

float observations in the upper 30 m at intervals of 5 days, 5-m depth, 3° latitude, and 10° longitude of the GLODAPv2 1992–2013 observations (Fig. 6.10f, red and blue pluses for 2017 and 2014–16 float data comparisons, respectively).

The two estimates reveal consistent trends (determined by least-squares fit) in pH, hence ocean acidification. The first approach resulted in an acidification rate of -0.0023 yr^{-1} ; for the second method the rate was -0.0025 yr^{-1} and -0.0028 yr^{-1} for the 2014–16 and 2017 float data comparisons, respectively, implying either the 2017 floats sampled lower pH (than was sampled in 2014 to 2016) or the 2017 floats captured different spatial variability. These results are nevertheless consistent with previous observations based on individual hydrographic lines (Rios et al. 2015; Williams et al. 2015) or based on predictions from coupled models. Faster acidification rates in the Southern Ocean compared to the global average ($\sim -0.0017 \text{ year}^{-1}$) expected due to low carbonate ion concentrations in the Southern Ocean (McNeil and Matear 2008; Orr et al. 2005). Nonetheless, there is considerable spatial and temporal variability in surface ocean pH, both in observed and as predicted with coupled climate models (Russell et al. 2018), but as the float record expands and lengthens, both the assessment and prediction of the spatial and temporal variability in acidification rates will improve.

g. 2017 Antarctic ozone hole—N. Kramarova, P. A. Newman, E. R. Nash, S. E. Strahan, C. S. Long, B. Johnson, M. L. Santee, I. Petropavlovskikh, G. O. Braathen, and L. Coy

Severe ozone depletion in the Antarctic stratosphere has been observed every austral spring since the early 1980s (WMO 2014) and is caused by heterogeneous chemical reactions with human-made chlorine- and bromine-containing compounds. As much as 98% of the ozone in the lower stratosphere around 70 hPa is destroyed in September–October. As a result of regulations set in place by the Montreal Protocol and its amendments, levels of chlorine from ozone depleting substances have gradually declined, and springtime Antarctic ozone is beginning to show signs of recovery (WMO 2014).

The 2017 Antarctic ozone hole was the second smallest since 1988, with an area of 17.4 million km^2 (or 6.7 million mi^2) averaged from 7 September to 13 October, the period of greatest ozone depletion. The ozone hole area is defined as the area with total column ozone values less than 220 Dobson units (DU). Figure 6.11d displays the daily areal coverage of the ozone hole for 2017 (black curve). The area started expanding at the beginning of August, with

a dip due to stratospheric warming in mid-August. It increased until another stratospheric warming stopped the expansion in mid-September, reaching a 19.6 million km^2 peak on 11 September, and then declined slowly into October and disappeared on 19 November. The warmings prevented the hole from

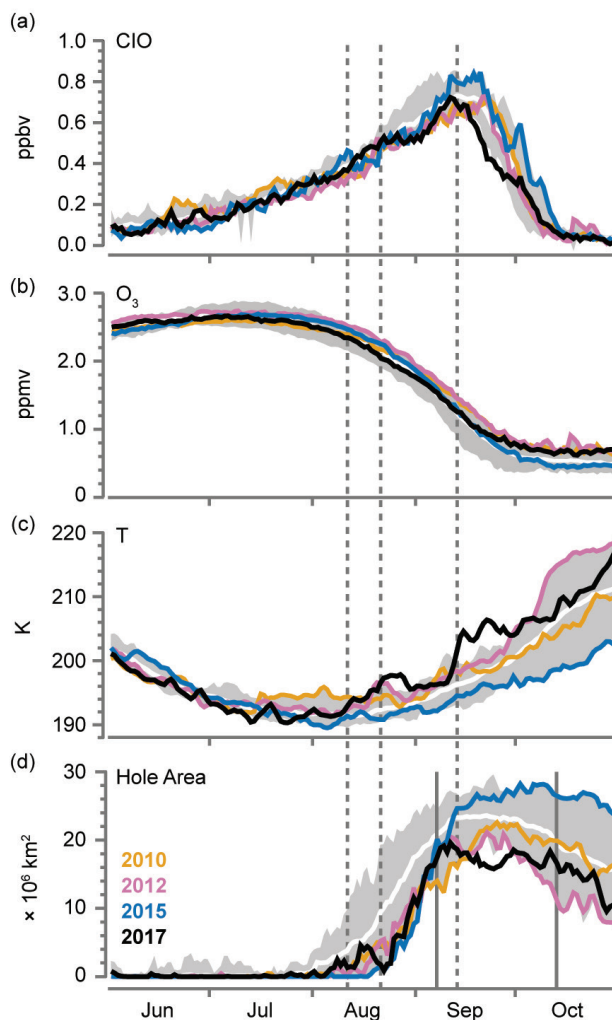


FIG. 6.11. Antarctic vortex-averaged concentrations of: (a) CIO and (b) ozone from *Aura* MLS (updated from Manney et al. 2011). These MLS averages are made inside the polar vortex on the 440-K isentropic surface ($\sim 18 \text{ km}$ or 65 hPa). (c) Temperature on the 440-K isentropic surface over Antarctica ($60^\circ\text{--}90^\circ\text{S}$) from MERRA-2 (Gelaro et al. 2017). (d) Ozone hole area based on Ozone Monitoring Instrument (OMI) and Ozone Mapping and Profiler Suite (OMPS) satellite observations. Four years are shown: 2010 (orange), 2012 (pink), 2015 (blue), and 2017 (black). The white line shows the daily average and the gray shading shows the daily ranges for 2005–16. The vertical solid lines indicate the averaging period for Fig. 6.13, while the vertical dashed lines indicate the dates of maximum wave forcing for the stratospheric warming events in 2017.